Advances in Industrial and Manufacturing Engineering 8 (2024) 100141

Contents lists available at ScienceDirect

Advances in Industrial and Manufacturing Engineering

journal homepage: www.sciencedirect.com/journal/advances-in-industrial-and-manufacturing-engineering

Introducing a novel sheet test specimen for biaxial stretching under uniaxial loading

Rui F.V. Sampaio [a], João P.M. Pragana [a], Ivo M.F. Bragança [a,b], Carlos M.A. Silva [a], Paulo A. F. Martins [a,*]

[a] IDMEC, Instituto Superior Técnico, Universidade de Lisboa, Portugal
[b] CIMOSM, Instituto Superior de Engenharia de Lisboa, Instituto Politécnico de Lisboa, Portugal

ARTICLE INFO

Keywords:
Diagonal-cruciform test specimen
Sheet formability
Finite element method
Experimentation

ABSTRACT

This paper introduces a novel sheet test specimen that plastically deforms under biaxial stretching when subjected to uniaxial loading in conventional testing machines. The specimen was designed using finite element simulation and consists of a two-dimensional reticular structure with interconnected arms in the form of triangles that converge at the center and are connected to full-width sheets at the specimen's ends. Accumulation of damage at the center is ensured through spherical cups that are milled at opposite sheet surfaces. Experimental strain loading paths obtained by digital image correlation confirm the capability of the novel sheet test specimen to provide biaxial stretching strain paths. This is achieved under friction-independent conditions and without requiring complicated multiaxial setups and machines, provided appropriate values of the inner and outer angles of the interconnected arms are used.

1. Introduction

In sheet forming, formability refers to a material's ability to undergo plastic deformation without failure, such as wrinkling, necking, or fracture. Understanding formability is crucial for designing processes and tooling systems. By integrating formability knowledge with advanced numerical simulation techniques and accumulated experience, engineers can validate their designs from technical, economic, and environmental standpoints before fabricating the tooling and initiating production.

The first research works on formability in sheet forming are attributed to Keeler (1965), and Goodwin (1968), who introduced circle grid analysis (CGA) and plotted the evolutions of the major and minor in-plane strains in the first (tension-tension) and second (tension-compression) quadrants of principal strain space, respectively. Since then, principal strain space has been the preferred graphical representation to plot strain loading paths and material formability limits by necking (Paul, 2021) and fracture (Isik et al., 2014) in sheet forming.

For determining the formability limits by necking, also known as forming limit curves (FLCs), there are standards like the ISO 12004-2 (2021) that typically require the utilization of Nakajima (Nakajima et al., 1968) (Fig. 1a) or Marciniak (1965) tests.

Unlike the formability limits by necking, there are no standardized methods for determining the formability limits by fracture, also known as fracture forming limits (FFLs). However, commonly used procedures involve a combination of Nakajima tests and uniaxial loading tests performed on specimens with various geometries. These tests cover both crack opening modes by tension (mode I of fracture mechanics) and in-plane shear (mode II of fracture mechanics) (Magrinho et al., 2019) (Fig. 1b).

Nakajima tests are primarily utilized to obtain biaxial stretching strain paths up to fracture, a condition not replicated by the uniaxial loading tests, but they require specialized tool sets and are highly sensitive to friction. The sensitivity to friction often results in cracks initiating away from the specimen's pole, prompting exploration of alternative solutions such as the utilization of cruciform test specimens.

In the past years, several cruciform test specimens and procedures have been proposed in the literature and systematized in comprehensive review papers (Xiao, 2019). Despite differences in the design of the specimens aimed at locating fractures at the center and avoiding premature failure along the specimen's arms, they all require access to multiaxial testing machines, which are more expensive than uniaxial

* Corresponding author.
E-mail addresses: rui.f.sampaio@tecnico.ulisboa.pt (R.F.V. Sampaio), joao.pragana@tecnico.ulisboa.pt (J.P.M. Pragana), ibraganca@dem.isel.ipl.pt (I.M.F. Bragança), carlos.alves.silva@tecnico.ulisboa.pt (C.M.A. Silva), pmartins@tecnico.ulisboa.pt (P.A.F. Martins).

https://doi.org/10.1016/j.aime.2024.100141
Received 18 March 2024; Received in revised form 17 April 2024; Accepted 18 April 2024
Available online 19 April 2024

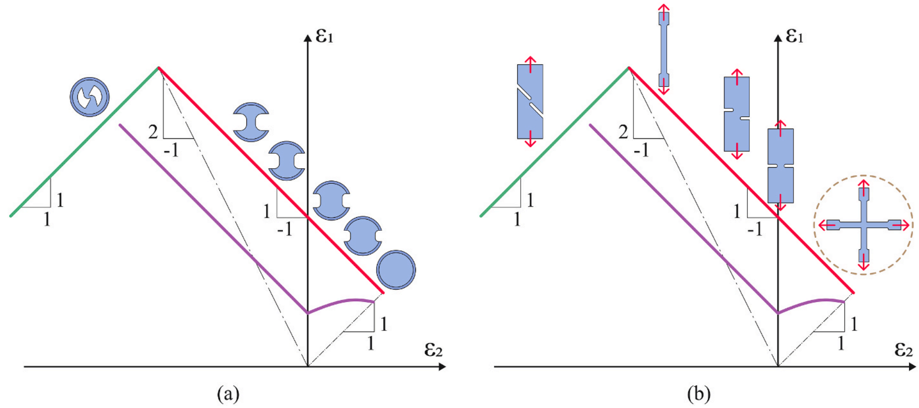

Fig. 1. Forming limit diagram in sheet forming using (a) Nakajima test specimens and (b) various uniaxial and biaxial test loading specimens.

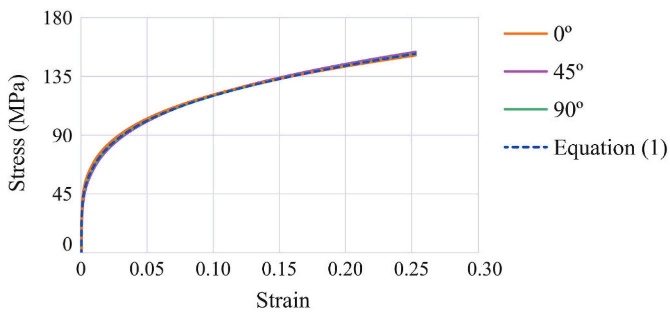

Fig. 2. Flow stress of aluminum AA 6082-O.

testing machines and may not always be readily available.

The primary objective of this paper is to introduce a novel sheet test specimen capable of providing biaxial stretching strain paths under uniaxial loading. Unlike Nakajima and Marciniak tests, the novel sheet test is friction-independent, with its specimen design inspired by cruciform test specimens recently published in the literature. Specifically, it draws inspiration from the design of Song et al. (2017) combined with that of Ha et al. (2019), which features symmetric thickness reduction at the center.

Although other designs with primary and secondary zones of thickness reduction at the center, aimed at better concentrating deformation and failure (Zhang et al., 2021), could have been used as inspiration for the design of the novel sheet test specimen, they were not considered because the focus of this first paper was on demonstrating its ease and feasibility in providing biaxial stretching strain paths using conventional uniaxial testing machines commonly found in mechanical characterization laboratories.

The design of the novel sheet test specimens is supported by finite element simulations, utilizing in-house computer software, and by experimental tests employing digital image correlation (DIC) measurements (Peters and Ranson, 1982). The latter were used to obtain the proof-of-concept by confirming the ability of the novel sheet test specimens to provide strain loading paths in the first quadrant (biaxial stretching) of principal strain space when subjected to uniaxial loading.

2. Experimentation

2.1. Material characterization

The experimental work was carried out on AA6082-O aluminum sheets with a thickness of 2 mm. The flow stress of the material at ambient temperature was determined through tensile tests using an INSTRON 4507 universal testing machine. These tests were performed within the research unit (Colaço, 2023) following the ASTM E8 standard (ASTM, 2022) and Fig. 2 displays the results obtained for the specimens extracted at 0°, 45°, and 90° inclination to the rolling direction.

The results depicted in Fig. 2 led to the assumption that aluminum AA6082-O is isotropic, with a flow stress that can be approximated by the following Ludwik–Hollomon strain hardening model,

$$\sigma = 215\varepsilon^{0.25} \qquad (1)$$

2.2. Formability tests and methodology

The formability limits by necking (FLC) and fracture (FFL) of aluminum AA6082-O were previously determined by Colaço (2023) using a combination of Nakajima and uniaxial loading tests that made

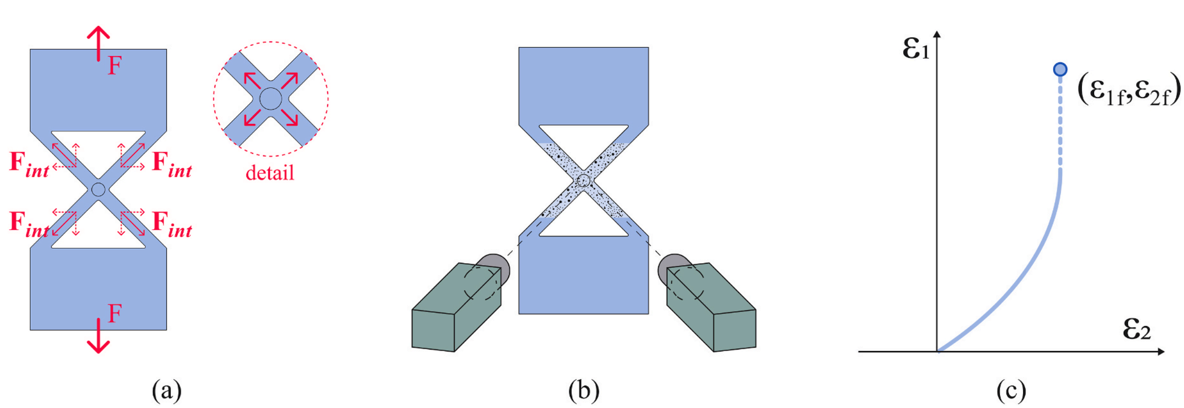

Fig. 3. Schematic representation of the diagonal-cruciform sheet test specimen, illustrating (a) the working principle resulting from the decomposition of the external uniaxial force F along the arms, (b) the experimental setup utilized by the DIC system, and (c) a typical evolution of strain paths in principal strain space.

Table 1
Main geometric parameters of the diagonal-cruciform test specimens.

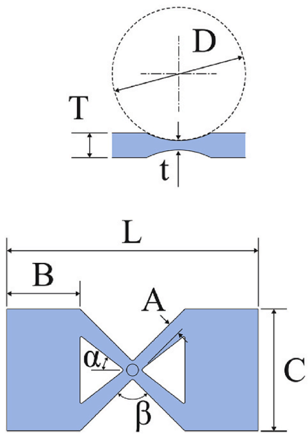

Dimensions (mm)
$A = 5$
$B = 30$
$C = 50$
$L = 103$
$D = 10$
$T = 2$
$t = 0.75$
$\alpha = 30^\circ, 37.5^\circ, 45^\circ$
$\beta = 75^\circ, 90^\circ$

use of tension, double-notched and staggered specimens. These limits will serve as reference values to validate the results obtained with the novel sheet test specimen.

The novel sheet test specimen, hereafter referred to as 'diagonal-cruciform', consists of interconnected arms in the form of triangles, creating a two-dimensional reticular structure, linked to full-width sheets at the specimen's ends (refer to Fig. 3). The arms join at the center to create a deformable region that is subjected to biaxial tension along the arms caused by the internal axial forces F_{int} resulting from the decomposition of the external uniaxial force F applied at the specimen ends (refer to Fig. 3a).

Fig. 3b illustrates the experimental setup utilized by the DIC system to determine the evolution of the in-plane strains with time $\varepsilon_1(t), \varepsilon_2(t)$ and to plot their combined evolution $\varepsilon_1 = f(\varepsilon_2)$ in principal strain space, after removing the time dependency.

The strains at fracture $(\varepsilon_{1f}, \varepsilon_{2f})$ are determined from the variation in thickness up to fracture (Embury and Duncan, 1981), assuming plane strain loading conditions $d\varepsilon_2 \approx 0$ (Atkins, 1996), either after necking (if, present) or after the last measurement of the DIC system (in the absence of necking),

$$(\varepsilon_2)_f = (\varepsilon_2)_n \tag{2}$$

$$(\varepsilon_1)_f = -(\varepsilon_2)_f - (\varepsilon_3)_f = -(\varepsilon_2)_f - \ln\frac{t_f}{t_0} \tag{3}$$

In the above equations, the subscripts n and f represent values at necking and fracture, respectively, while t denotes the sheet thickness.

The validation of the proof-of-concept required designing an experimental work plan involving diagonal-cruciform test specimens machined from AA6082-O sheets with a thickness of 2 mm. All the specimens had their centers milled with a 10 mm ball nose end mill to create two opposite spherical cups, with a minimum thickness of 0.75 mm between them, to induce plastic strain and damage accumulation at the center. A positioning jig was utilized to ensure symmetry between

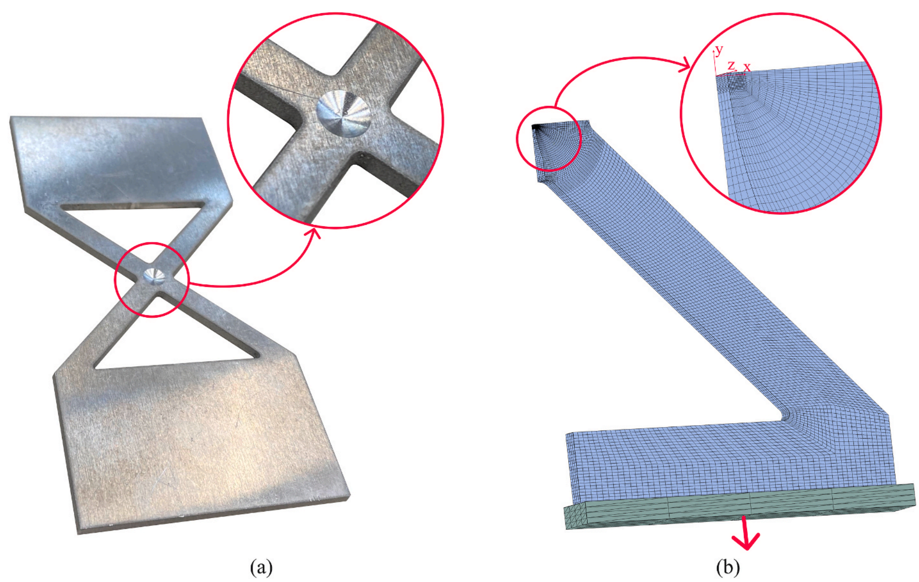

Fig. 4. The diagonal-cruciform sheet test specimen: (a) photograph and (b) finite element model with details of the center regions.

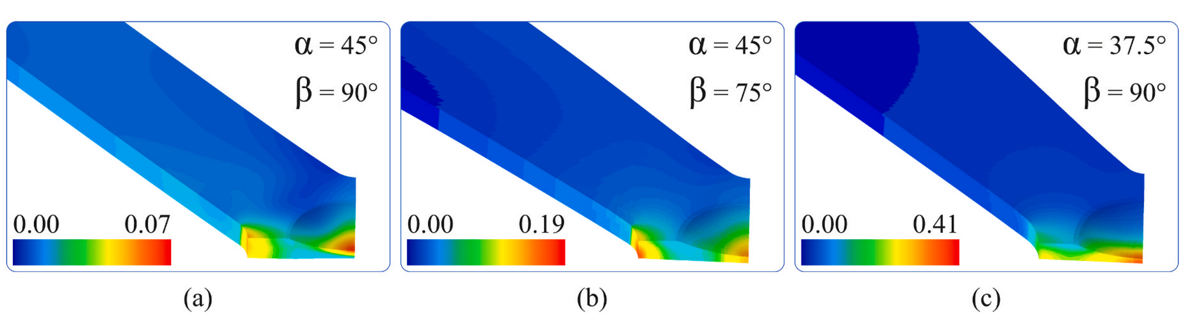

Fig. 5. Finite element distribution of damage using the McClintock fracture criterion for diagonal-cruciform test specimens with inner and outer arm angles respectively set to (a) $\alpha = 45^\circ$, $\beta = 90^\circ$, (b) $\alpha = 45^\circ$, $\beta = 75^\circ$, and (c) $\alpha = 37.5^\circ$, $\beta = 90^\circ$, after 2.9 mm displacement of the grips.

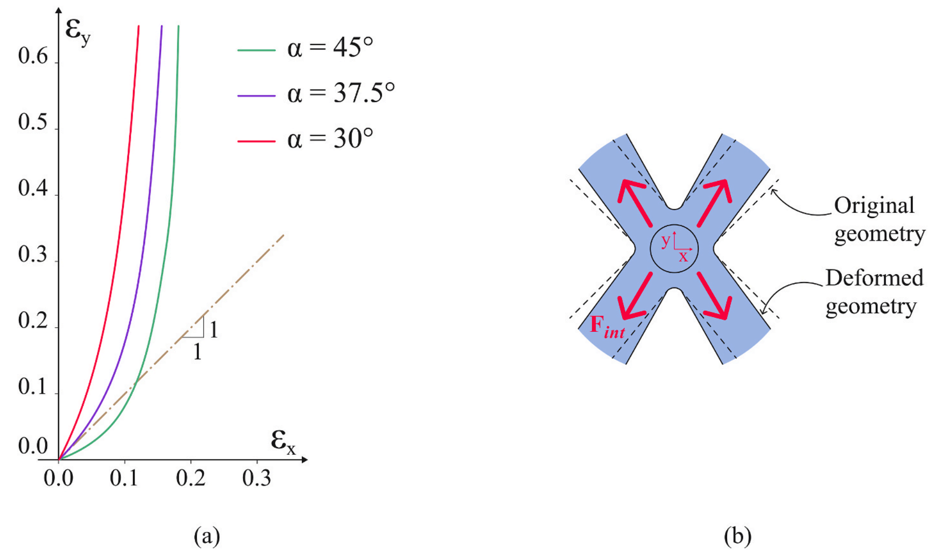

Fig. 6. (a) Finite element predicted strain loading paths in $\varepsilon_y = f(\varepsilon_x)$ for diagonal-cruciform test specimens with an outer arm angle set at $\beta = 90^\circ$ and various inner arm angle values of $\alpha = 30^\circ, 37.5^\circ$ and 45°. (b) schematic representation of the changes in the reticular structure's geometry of the specimen subjected to uniaxial loading.

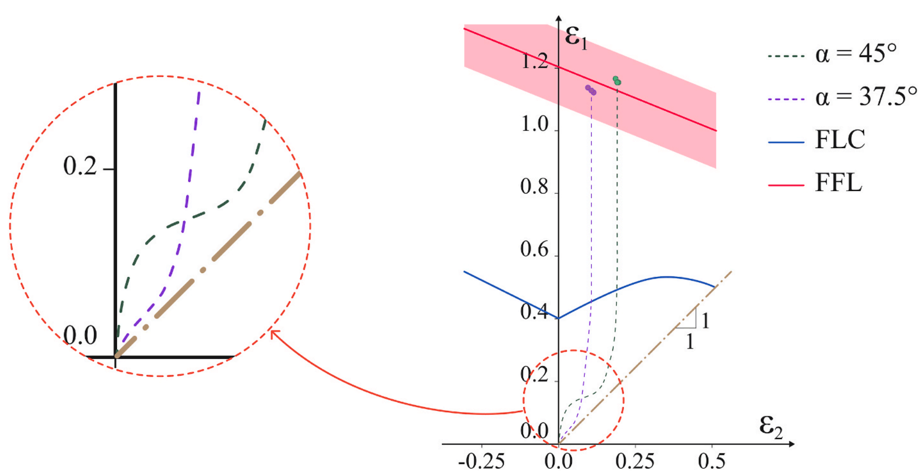

Fig. 7. Experimental strain loading paths in principal strain space $\varepsilon_1 = f(\varepsilon_2)$ for the diagonal-cruciform specimens having $\alpha = 45^\circ$ (green) and $\alpha = 37.5^\circ$ (purple) with a detail of the evolutions at small strains. The FLC (blue) and FFL (red) were obtained from the work of Colaço (2023). (For interpretation of the references to colour in this figure legend, the reader is referred to the Web version of this article.)

the opposing machined faces of the specimens.

Table 1 provides the main geometric parameters of the diagonal-cruciform test specimens used in the experiments. Most of the parameters were kept constant, apart from the inner α and outer β angles, which were allowed to vary to achieve different strain loading paths, as will be shown later in the 'Results and Discussion' section.

Preliminary work with geometries having larger arm widths (A = 12 mm) was also performed, but the resulting specimens were found inadequate to concentrate the accumulation of damage at the center.

DIC measurements of the in-plane strains over time, at the center of the diagonal-cruciform specimen were performed with a Dantec Dynamics (model Q-400 3D) commercial system, equipped with two 6-megapixel resolution cameras featuring 50.2 mm focal lenses and f/8 aperture (refer to Fig. 3b). The use of 10 mm spacers in the lenses to diminish the minimum focusing distance allowed increasing detail in close-up shots of the center region of the specimen. The regions of interest were painted with a stochastic black dot pattern, covering approximately 40% of the previously painted white background. These regions were illuminated with a spotlight during testing, and images were captured by the two cameras at a shutter frequency of 10 Hz (equivalent to 10 images per second).

The evolutions of the strain loading paths in principal strain space $\varepsilon_1 = f(\varepsilon_2)$ (Fig. 3c) were automatically obtained through combination of the evolutions of the major and minor in-plane strains with time using an open-source software that was recently developed by the authors (Sampaio et al., 2023).

2.3. Numerical simulations

The diagonal-cruciform sheet test specimens were numerically simulated with the in-house computer software i-form, which is built upon the quasi-static finite element flow formulation (Nielsen and Martins, 2021). The material of the specimens was assumed to be isotropic, following the Levy-Mises constitutive equations, with a flow stress given by equation (1). The geometries of the specimens were discretized with approximately 50,000 three-dimensional hexahedral elements, considering the symmetry planes xy, yz, and xz (see Fig. 4b).

The grips that hold and apply a constant velocity to the specimen's

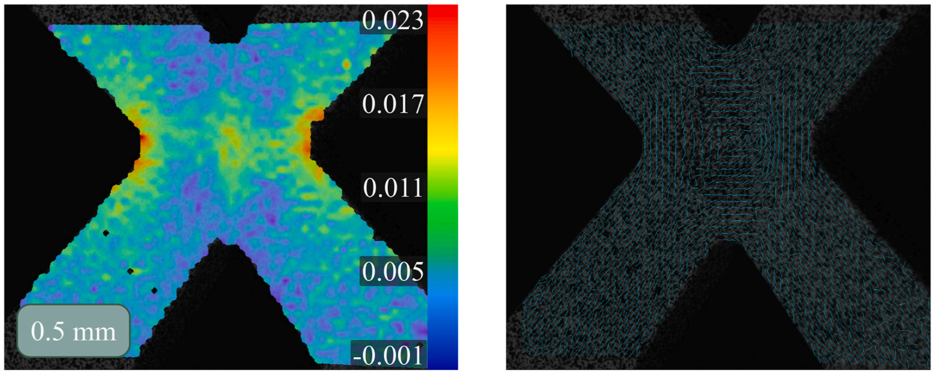

(a)

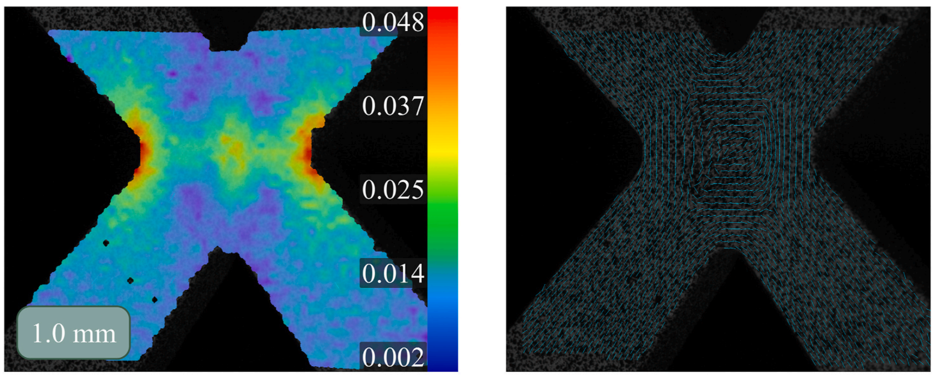

(b)

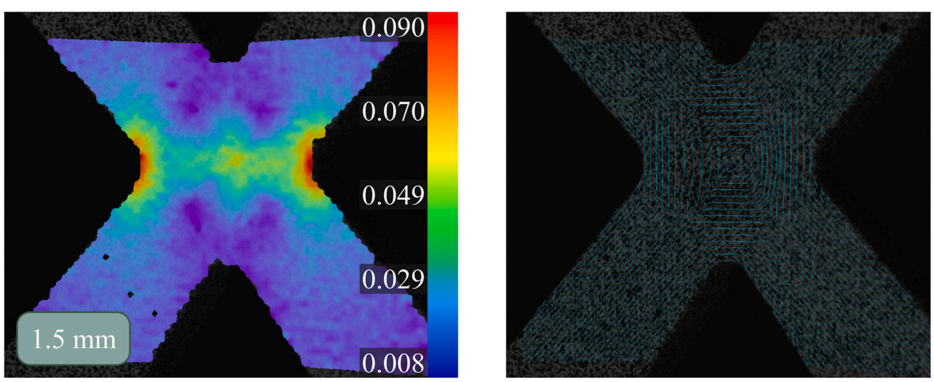

(c)

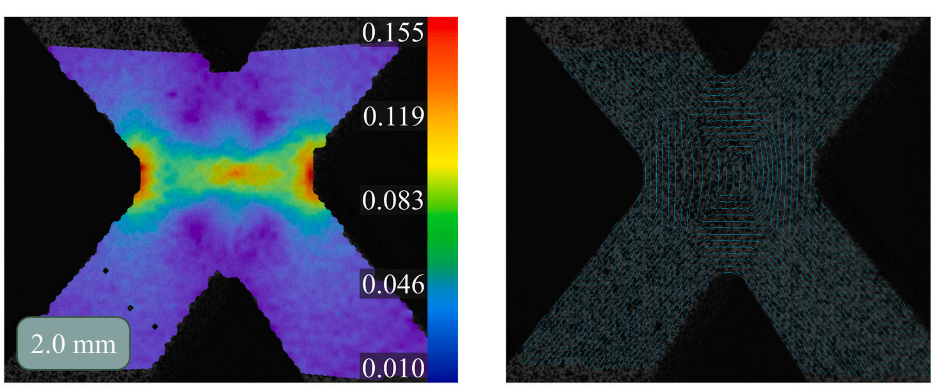

(d)

Fig. 8. DIC-defined ε_1 distributions with direction vectors in a specimen with $\alpha = 37.5^\circ$ and $\beta = 90^\circ$ for: (a) 0.5 mm, (b) 1.0 mm, (c) 1.5 mm, and (d) 2.0 mm of vertical displacement.

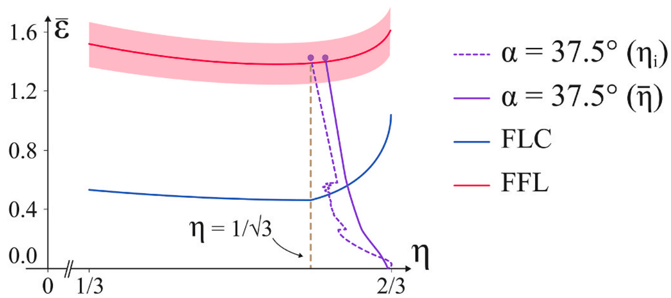

Fig. 9. Experimental loading paths in the effective strain vs. stress triaxiality space $\bar{\varepsilon} = f(\eta)$ for the diagonal-cruciform specimen with $\alpha = 37.5°$ and $\beta = 90°$, using instantaneous η_i and weighted average $\bar{\eta}$ stress triaxiality values.

boundaries were discretized by means of spatial triangular surface elements and assumed to be rigid objects. The nodes of the specimen in contact with these grips were fixed.

Damage accumulation was modelled using the McClintock (1968) fracture criterion, as it accounts for crack opening by tension (mode I of fracture mechanics) in the tension-tension region of principal strain space, where fracture strains are likely to occur (Martins et al., 2014).

3. Results and discussion

3.1. Design of the diagonal-cruciform test specimen

Design of the diagonal-cruciform test specimen involved finite element simulations to understand the influence of the inner α and outer β arm angles on the strain loading path and accumulation of ductile damage in the center region of the specimen. By firstly keeping the inner arm angle constant at $\alpha = 45$ °, results in Fig. 5a and b allow us to conclude that the accumulation of ductile damage at the center requires using larger outer arm angles (e.g., $\beta = 90°$), as smaller angles (e.g., $\beta = 75°$) shift the maximum accumulation of damage from the center to the periphery (see Fig. 5a and b).

Then, by keeping the outer arm angle constant at $\beta = 90°$, results show an increase in damage accumulation as the inner angle of the specimen decreases towards $\alpha = 37.5°$. This is accompanied by a strain loading path shift in $\varepsilon_y = f(\varepsilon_x)$ (Fig. 6a) from equibiaxial stretching during the initial testing stage to biaxial stretching throughout the rest of the test, due to progressive change in the reticular structure's geometry, which causes the internal axial forces F_{int} to gradually rotate towards the longitudinal direction (Fig. 6b).

The use of smaller values of the inner arm angle (say, $\alpha = 30°$) will shift the strain loading paths towards plane strain deformation (Fig. 6a), while still maintaining the maximum accumulated damage at the center of the test specimen.

Finally, finite element simulations also indicate that the test specimen with an inner arm angle $\alpha = 45$ ° should not be used because it initially exhibits $\varepsilon_x > \varepsilon_y$, but with continued deformation, the strain loading path crosses the straight line of equibiaxial stretching and evolves to $\varepsilon_y > \varepsilon_x$. This implies that both major and minor strain directions will alter during the test, as demonstrated in the following section, where plots of $\varepsilon_1 = f(\varepsilon_2)$ in principal strain space will be used instead of $\varepsilon_y = f(\varepsilon_x)$.

3.2. Experimental validation of the proof-of-concept

The previous section allows concluding that the outer arm angle β should ideally be set to 90 ° while the inner arm angle α can vary within a certain range. To better understand the influence of α on the strain loading paths, a series of experiments were carried out with two different geometries of the diagonal-cruciform specimen, having $\alpha = 37.5°$ and $\alpha = 45°$.

The experimental strain loading paths up to fracture were determined according to the methodology described in Section 2.2 and the results are plot in Fig. 7, which also includes the FLC and FFL previously determined by Colaço (2023). As seen, the fracture strains provided by the two diagonal-cruciform specimens occur under biaxial stretching, with values that are in good agreement with the previously determined FFL.

The major differences between the results provided by the two diagonal-cruciform specimens are attributed to plastic deformation at the center region, which begins under plane strain deformation when $\alpha = 45°$, or near equibiaxial stretching when $\alpha = 37.5°$, and finishes under biaxial stretching for both type of specimens. This explains why the diagonal-cruciform specimen with $\alpha = 45°$ undergoes a shift in strain from $\varepsilon_x > \varepsilon_y$ into $\varepsilon_y > \varepsilon_x$ after the initial stages of deformation. The shift is clearly visible in principal strain space $\varepsilon_1 = f(\varepsilon_2)$, when the initial loading path, close to plane strain, bends towards equibiaxial stretching, in close compatibility with the $\varepsilon_y = f(\varepsilon_x)$ evolution of Fig. 6, in which the strain loading path crosses the straight line of equibiaxial stretching.

In contrast, there is practically no shift for the strain loading path obtained for the diagonal-cruciform specimen with $\alpha = 37.5°$, which mainly follows the straight line of equibiaxial stretching until it bends towards biaxial stretching with $\varepsilon_1 > \varepsilon_2$. This is confirmed by the evolution of the DIC-defined ε_1 direction vectors for different deformation stages that is disclosed in Fig. 8.

Indeed, at a vertical displacement of 0.5 mm, the ε_1 direction vectors exhibit some misalignment with a tendency to encircle the central spherical cup region (Fig. 8a). Upon reaching a displacement of 1.0 mm (Fig. 8b), the direction vectors at the center begin to align in an inclined direction, indicative of the equibiaxial stretching loading path that is observed during the initial stages of deformation (Fig. 7). Subsequently,

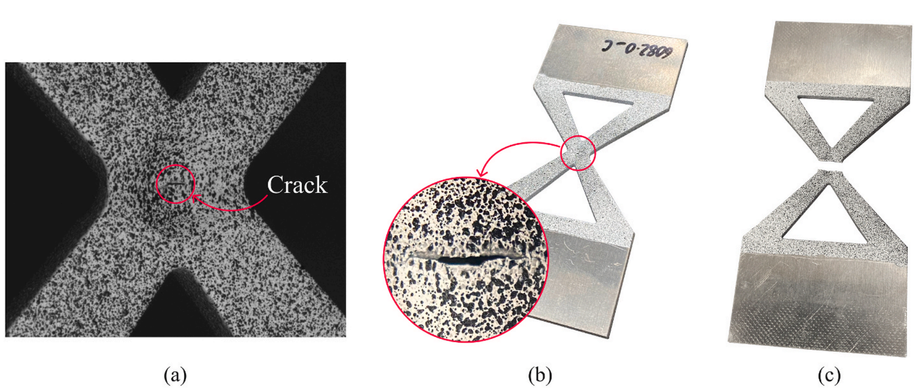

Fig. 10. (a) Crack initiation observed with DIC, (b) photograph and macro shot detail of a specimen exhibiting cracking but no separation, and (c) photograph of a cracked specimen fully separated.

at a displacement of 1.5 mm (Fig. 8c), the direction vectors gradually rotate towards the vertical direction, compatible with the deviation of the strain loading path from equibiaxial to biaxial stretching. Finally, at a displacement of 2.0 mm (Fig. 8d), the direction vectors at the center attain steady-state conditions as they align vertically and close to plane strain deformation along the horizontal direction.

Fig. 9 shows two loading path evolutions for the diagonal-cruciform specimen with $\alpha = 37.5^\circ$ and $\beta = 90^\circ$, in the effective strain vs. stress-triaxiality space $\bar{\varepsilon} = f(\eta)$. One evolution makes use of the instantaneous η_i stress triaxiality while the other makes use of the weighted average $\bar{\eta}$ stress triaxiality, which results from the piecewise treatment of the experimental loading path, as follows (Sampaio et al., 2023),

$$\bar{\eta} = \frac{\sum_{i=0}^{N} (\eta_i \Delta\bar{\varepsilon}_i)}{\bar{\varepsilon}} \tag{4}$$

In the above equation, N is the total number of measurements performed by the DIC system, $\Delta\bar{\varepsilon}_i$ is the increment of effective strain between consecutive measurements and $\bar{\varepsilon}$ is the total effective strain calculated from the in-plane strain values $(\varepsilon_1, \varepsilon_2)$ obtained from the DIC system.

As observed in Fig. 9, both evolutions closely align, providing final stress triaxiality values of $\eta_f = 0.577$ and $\bar{\eta}_f = 0.594$, which are in close agreement with the assumption of plane strain loading conditions $d\varepsilon_2 \approx 0$ after the last measurement of the DIC system (without signs of necking prior to fracture).

The experimental validation of the proof-of-concept concludes with the observation of Fig. 10, which demonstrates that fracture initiates at the center spherical cup (Fig. 10a and b), in close agreement with the finite element prediction of accumulated damage (refer to Fig. 5c). Subsequently, as deformation progresses, cracks propagate and give rise to the separation of the specimen into two halves (Fig. 10c).

4. Conclusions

The novel diagonal-cruciform sheet test specimen can be successfully used to obtain strain loading paths up to fracture in the tension-tension quadrant of principal strain space. The specimen can be easily tested in conventional uniaxial testing machines, eliminating the need for special-purpose experimental setups or multiaxial testing machines.

Variations in the inner arm angle α of the reticular structure of the specimen allow obtaining different values of strain at fracture, contributing to the characterization of the fracture forming limits (FFLs) under biaxial stretching. However, the values of the inner arm angle α should not approach 45° to avoid a shift between major and minor strain directions at the early stages of deformation due to plane strain compression along the horizontal direction. Fracture at the spherical cup region of the specimen occurs after crack opening and propagation by tension due to the accumulation of ductile damage.

CRediT authorship contribution statement

Rui F.V. Sampaio: Writing – review & editing, Writing – original draft, Visualization, Validation, Software, Resources, Methodology, Investigation, Formal analysis, Conceptualization. **João P.M. Pragana:** Writing – review & editing, Visualization, Supervision, Methodology, Investigation, Formal analysis, Conceptualization. **Ivo M.F. Bragança:** Writing – review & editing, Supervision, Resources, Methodology, Investigation, Formal analysis, Conceptualization. **Carlos M.A. Silva:** Writing – review & editing, Supervision, Resources, Methodology, Investigation, Formal analysis, Conceptualization. **Paulo A.F. Martins:** Writing – review & editing, Writing – original draft, Supervision, Project administration, Methodology, Funding acquisition, Conceptualization.

Declaration of competing interest

The authors declare that they have no known competing financial interests or personal relationships that could have appeared to influence the work reported in this paper.

Data availability

Data will be made available on request.

Acknowledgments

The authors would like to acknowledge the support provided by Fundação para a Ciência e a Tecnologia (FCT) and IDMEC for its financial support via the project LAETA Base Funding (DOI: 10.54499/UIDB/50022/2020) and PTDC/EME-EME/0949/2020. Rui F.V. Sampaio would also like to acknowledge the support under the PhD Studentship 2022.12351.BD.

References

ASTM, 2022. ASTM E8/E8M-22: Standard Test Methods for Tension Testing of Metallic Materials. American Society for Testing and Materials, Wes Conshohocken, USA.
Atkins, A.G., 1996. Fracture in forming. J. Mater. Process. Technol. 56, 609–618. https://doi.org/10.1016/0924-0136(95)01875-1.
Colaço, B., 2023. Metodologia para a aplicação de estampagem incremental na manutenção de componentes de chapa metálica. Academia Militar, Lisbon, Portugal. MSc Thesis.
Embury, J.D., Duncan, J.L., 1981. Formability maps. Annu. Rev. Mater. Sci. 11, 505–521. https://doi.org/10.1146/annurev.ms.11.080181.002445.
Goodwin, G., 1968. Application of strain analysis to sheet metal forming problems in the press shop. SAE Trans. 77, 380–387. https://doi.org/10.4271/680093.
Ha, J., Baral, M., Korkolis, Y.P., 2019. Ductile fracture of an aluminum sheet under proportional loading. J. Mech. Phys. Solid. 132, 103685 https://doi.org/10.1016/j.jmps.2019.103685.
Isik, K., Silva, M.B., Tekkaya, A.E., Martins, P.A.F., 2014. Formability limits by fracture in sheet metal forming. J. Mater. Process. Technol. 214, 1557–1565. https://doi.org/10.1016/j.jmatprotec.2014.02.026.
ISO, 2021. ISO 12004-2: Metallic Materials – Sheet and Strip – Determination of Forming-Limit Curves – Part 2: Determination of Forming-Limit Curves in the Laboratory. International Organization for Standardization, Geneva, Switzerland.
Keeler, S.P., 1965. Determination of forming limits in automotive stampings. SAE Trans. 74, 1–9. https://doi.org/10.4271/650535.
Magrinho, J.P., Silva, M.B., Reis, L., Martins, P.A.F., 2019. Formability limits, fractography and fracture toughness in sheet metal forming. Materials 12, 1493. https://doi.org/10.3390/ma12091493.
Marciniak, Z., 1965. Stability of plastic shells under tension with kinematic boundary condition. Arch. Mechaniki Stosorwanej 17, 577–592.
Martins, P.A.F., Bay, N., Tekkaya, A.E., Atkins, A.G., 2014. Characterization of fracture loci in metal forming. Int. J. Mech. Sci. 83, 112–123. https://doi.org/10.1016/j.ijmecsci.2014.04.003.
McClintock, F.A., 1968. A Criterion for ductile fracture by the growth of holes. J. Appl. Mech. 35, 363–371. https://doi.org/10.1115/1.3601204.
Nakajima, K., Kikuma, T., Hasuka, K., 1968. Study on the formability of steel sheets. Yamata Technical Report 141–154. Report no. 264.
Nielsen, C.V., Martins, P.A.F., 2021. Metal Forming: Formability, Simulation, and Tool Design, first ed. Academic Press, New York, USA. https://doi.org/10.1016/C2020-0-02428-X.
Paul, S.K., 2021. Controlling factors of forming limit curve: a review. Adv. Ind. Manuf. Eng. 2, 100033 https://doi.org/10.1016/j.aime.2021.100033.
Peters, W.H., Ranson, W.F., 1982. Digital imaging techniques in experimental stress analysis. Opt. Eng. 21, 427–431. https://doi.org/10.1117/12.7972925.
Sampaio, R.F.V., Alexandre, N.S.M., Pragana, J.P.M., Bragança, I.M.F., Silva, C.M.A., Martins, P.A.F., 2023. A software for research and education in ductile damage. Adv. Ind. Manuf. Eng. 7, 100127 https://doi.org/10.1016/j.aime.2023.100127.
Song, X., Leotoing, L., Guines, D., Ragneau, E., 2017. Characterization of forming limits at fracture with an optimized cruciform specimen: application to DP600 steel sheets. Int. J. Mech. Sci. 126, 35–43. https://doi.org/10.1016/j.ijmecsci.2017.03.023.
Xiao, R., 2019. A review of cruciform biaxial tensile testing of sheet metals. Exp. Techniques 43, 501–520. https://doi.org/10.1007/s40799-018-00297-6.
Zhang, R., Shao, Z., Shi, Z., Dean, T.A., Lin, J., 2021. Effect of cruciform specimen design on strain paths and fracture location in equibiaxial tension. J. Mater. Process. Technol. 289, 116932 https://doi.org/10.1016/j.jmatprotec.2020.116932.